

AD-A104 804

NAVAL RESEARCH LAB WASHINGTON DC  
THE RAYLEIGH-TAYLOR AND KELVIN-HELMHOLTZ INSTABILITES IN TARGET--ETC(U)  
SEP 81 M H EMERY, J H GARDNER, J P BORIS

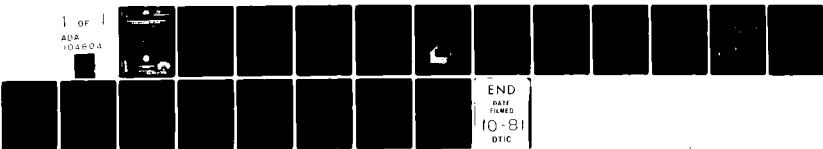
F/G 20/5

UNCLASSIFIED

NRL-NR-4626

NL

1 OF 1  
ADA  
104804



AD A104804





## THE RAYLEIGH-TAYLOR AND KELVIN-HELMHOLTZ INSTABILITIES IN TARGETS ACCELERATED BY LASER ABLATION

### I. INTRODUCTION

The Rayleigh-Taylor (R-T)<sup>1</sup> instability arises in the acceleration of a fluid by one of lower density. This instability may represent an obstacle to inertial confinement fusion by destroying the spherical symmetry of high aspect ratio imploding shells. The R-T instability causes corrugations on the ablation layer between the cold, high density shell and the hot, low density ablated material. These corrugations eventually grow nonlinearly to form the typical bubble-and-spike<sup>2</sup> structure. In addition the shear flow that develops as the bubble-and-spike structure evolves can lead to the Kelvin-Helmholtz (K-H)<sup>3,4</sup> instability.

Although much research has been applied to the study of the R-T instability in ablatively accelerated targets, a complete analytical theory that includes important physical phenomena such as finite density gradients, ablation effects, mass transfer, convection and finite thermal conduction is very difficult to perform and still does not exist. The nonlinear growth, turbulence and saturation processes are only now being investigated with computer codes, albeit with somewhat conflicting results.<sup>5,6,7</sup>

### II. MODEL

We report here on our investigation of the R-T, K-H instabilities in laser ablatively accelerated flat targets using the FAST2D<sup>8,9</sup> laser-shell simulation code. This is a fully two-dimensional Cartesian code with a sliding rezone Eulerian grid with variable grid spacing. The grid spacing is 0.25  $\mu\text{m}$  for 10 zones on either side of the ablation layer and increases uniformly to a 2.  $\mu\text{m}$  spacing for most of the rest of the grid. The finely

zoned region near the ablation layer is required in order to accurately resolve the steep density gradient. The zones in the underdense plasma beyond the critical surface and in the low density rear portion of the foil are stretched. The system has 40 zones transverse to the laser (y-direction) and 120 zones parallel (x-direction). The system is periodic in the transverse direction.

FAST2D solves the ideal hydrodynamic equations using the flux-corrected transport (FCT)<sup>10</sup> algorithms with a two-dimensional classical ( $T^{5/2}$ ) plasma thermal conduction routine. FAST2D accurately models rotational flow phenomena - a necessary criterion for any numerical code that intends to model the R-T instability into the nonlinear regime with its accompanying shear flow. It is important to realize that rotational flows occur with the R-T instability irrespective of the appearance of the K-H instability.<sup>11</sup>

The initial density, pressure and temperature profiles for an 20  $\mu\text{m}$  thick, plastic (CH) foil irradiated with an absorbed laser intensity of  $1.0 \times 10^{13} \text{ Wcm}^{-2}$  are generated from a one-dimensional, analytic, quasi-static equilibrium model.<sup>12</sup> The solutions have been shown to have provided an adequate steady-state with a one-dimensional laser-foil computer code.<sup>13</sup> A representative initial profile is illustrated in Fig. 1a. The initial conditions are assumed uniform in the transverse direction of the foil. A two-dimensional perspective plot of the mass density is shown in Fig. 1b.

The initial perturbation is obtained by perturbing the density profile at its peak. The first ten modes are excited with equal amplitudes and random phases corresponding to a total initial density perturbation of  $8\% \left( \frac{\rho_{\text{max}} - \rho_{\text{min}}}{\langle \rho \rangle} = 0.08 \right)$ . The longest wavelength excited is 100  $\mu\text{m}$ .

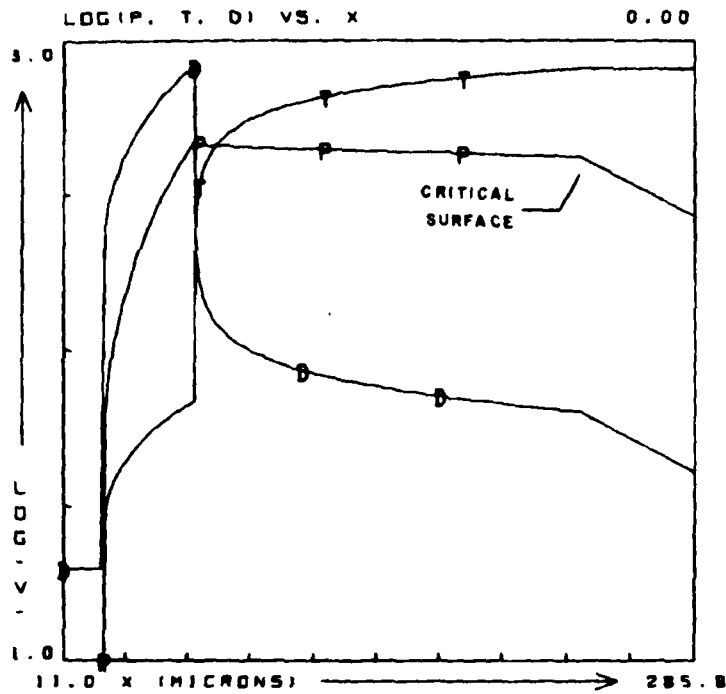


Fig. 1a — A semi-long plot of the initial pressure, density and temperature profiles of a thin, plastic foil

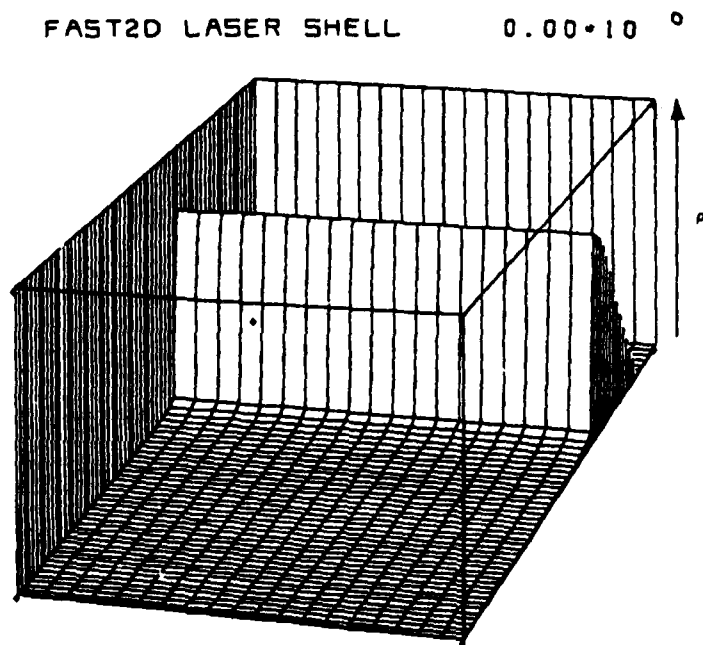


Fig. 1b — A two-dimensional perspective plot of the initial mass density. The laser is coming in from the front.

### III. NUMERICAL RESULTS

The amplitudes of the first five modes are shown in Fig. 2.  $M_k$  is the Fourier transform of the summed mass from the rear of the foil to the ablation edge for each y-coordinate. Note that the fifth mode [ $\lambda_5 = 20 \mu\text{m}$  (the foil thickness)] does not undergo any serious growth until after 7 nanoseconds. At this time the second and third modes undergo a slight but noticeable transition in their growth rate. It is at about this time that the bubble-and-spike formation becomes quite large and a strong shear flow develops which accelerates the growth of the spike. The growth saturates at about 9 nanoseconds and the foil fragments at 10.6 nanoseconds.

The growth rates for the first 5 modes are compared with the classical value,  $\gamma_c = (kg)^{1/2}$ , on Fig. 3. These growth rates are well below the classical values, in agreement with other time dependent calculations.<sup>14</sup> We also indicate growth rates obtained from a modified solution of Hsieh's<sup>15</sup> investigation of the R-T instability in boiling films. This solution includes mass and thermal transfer across the fluid layers. The growth rate can be expressed as

$$\gamma_H = \left[ \left( \frac{\alpha}{\rho_2} \right)^2 + kg \right]^{1/2} - \frac{\alpha}{\rho_2} ,$$

where  $\rho_2$  is the density of the "heavy" fluid and

$$\alpha \equiv \frac{G}{L} \left( \frac{1}{h_1} + \frac{1}{h_2} \right) .$$

$h_1$  ( $h_2$ ) is the depth of the "light" ("heavy") fluid,  $G$  is the thermal flux across the interface and  $L$  is the latent heat.  $L$  is determined by calculating the change in entropy across the ablation layer.

Fig. 4 shows a time sequence of density contours when the system is far into the nonlinear regime. The corresponding mass density perspective plots are shown in Fig. 5. The lines are contours of constant density in 10% increments of the maximum density ( $\rho_{\text{max}} = 0.71 \text{ gm/cm}^3$ ) counting from the outside inward. By 8 ns

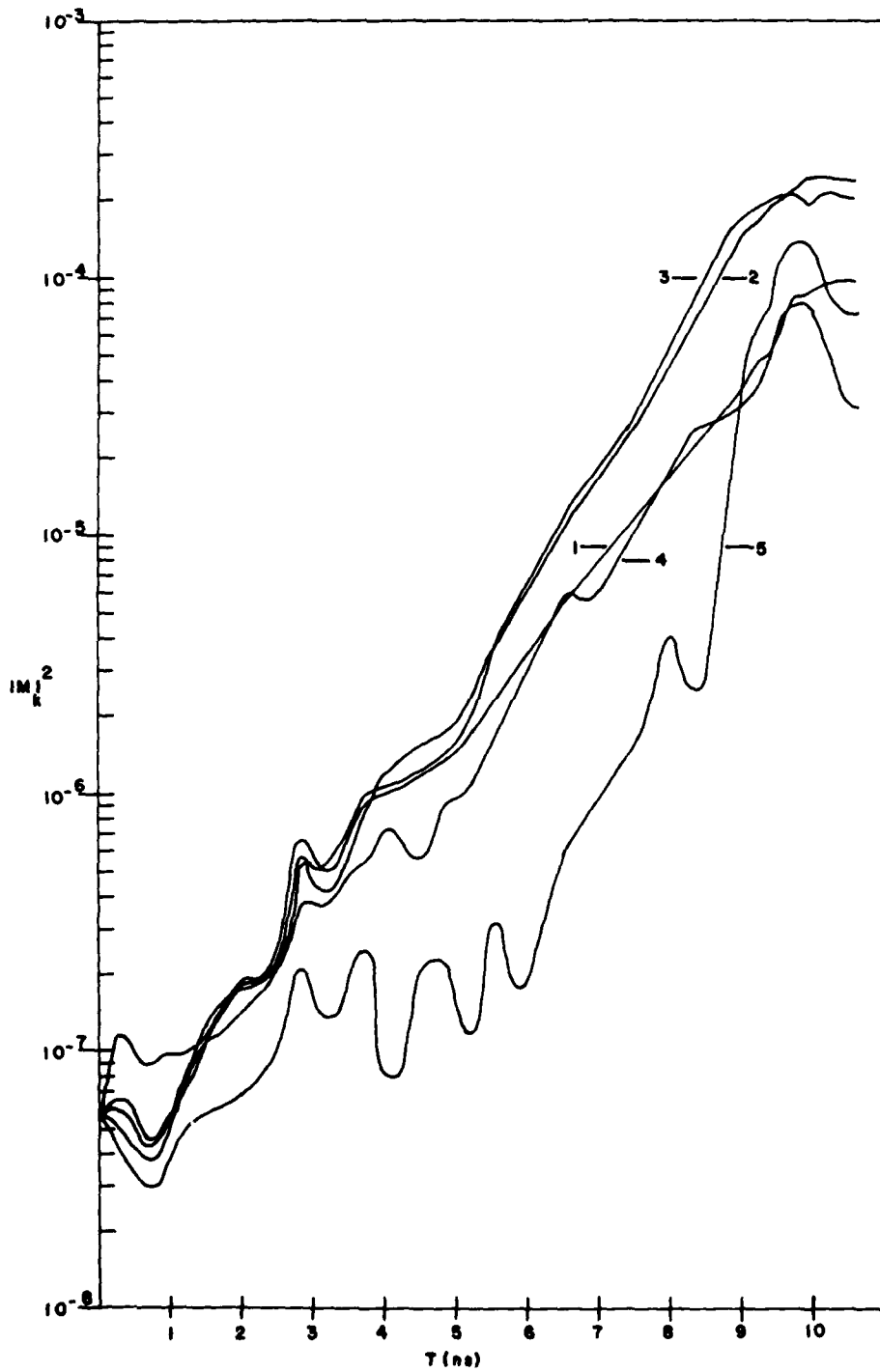


Fig. 2 — The square of the amplitude of the first five modes of the Rayleigh-Taylor instability as a function of time

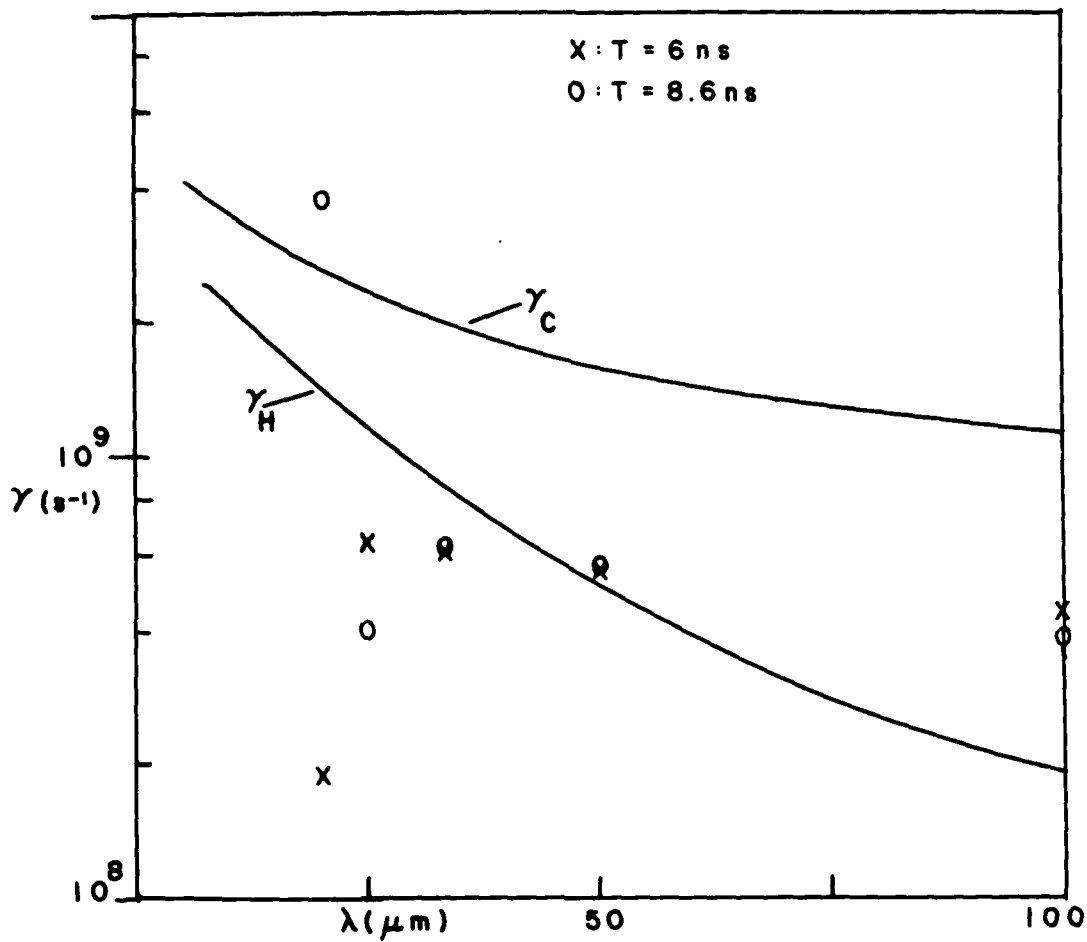


Fig. 3 — A comparison of the growth rates of the first 5 modes at two different times with the classical value ( $\gamma_c$ ) and a rate obtained from Hsieh<sup>15</sup> ( $\gamma_H$ )

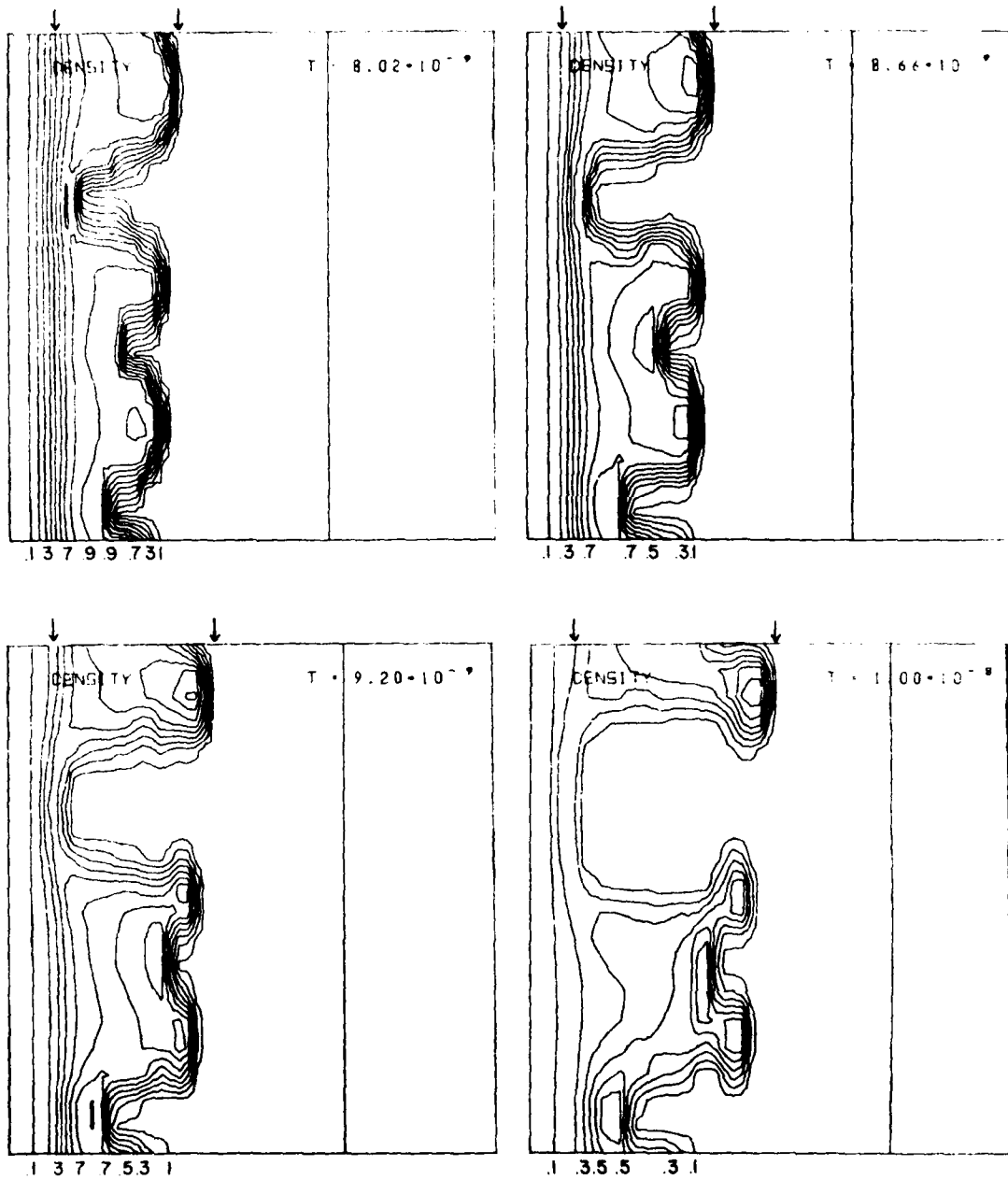
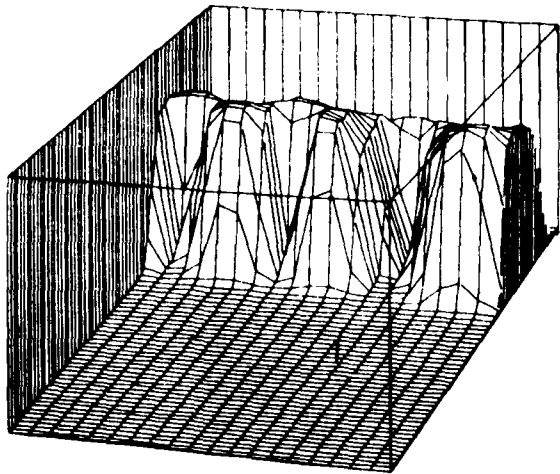
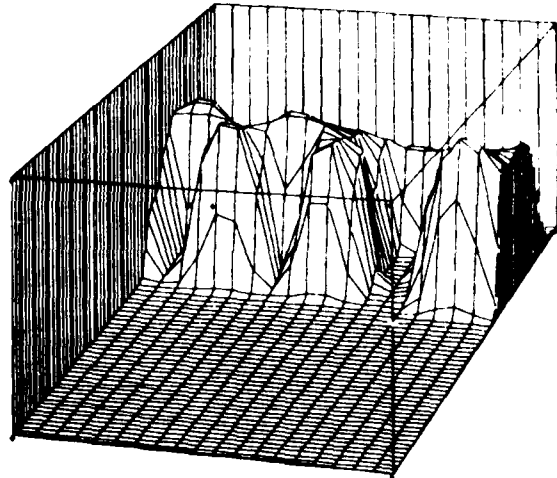


Fig. 4 -- Density contours at different times showing the development of the bubble-and-spike formation and the subsequent tip-spreading. The rightmost contour is the critical surface.

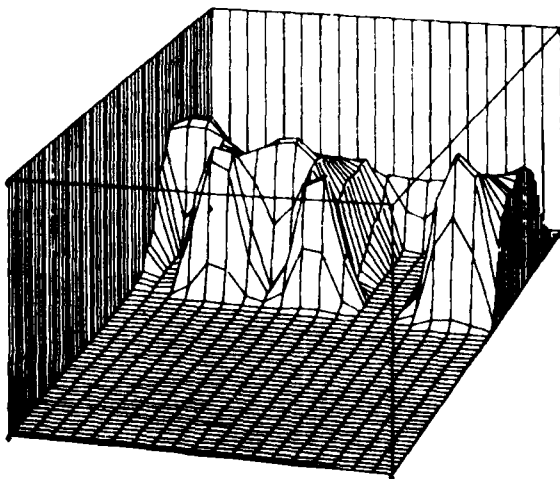
FAST2D LASER SHELL  $8.02 \cdot 10^{-9}$



FAST2D LASER SHELL  $8.66 \cdot 10^{-9}$



FAST2D LASER SHELL  $9.20 \cdot 10^{-9}$



FAST2D LASER SHELL  $1.00 \cdot 10^{-8}$

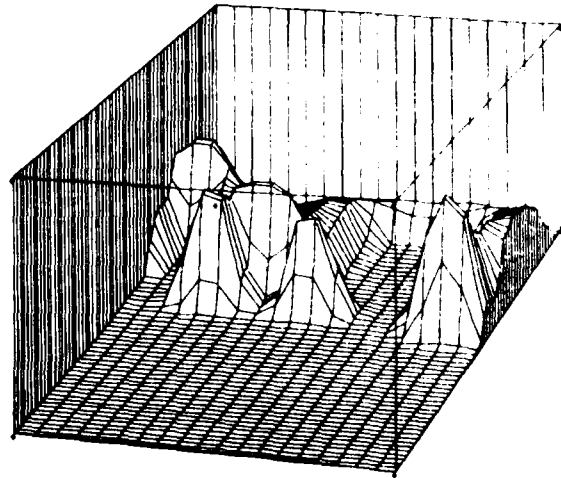


Fig. 5 — Two-dimensional mass density perspective plots for the same times as Fig. 4

the bubble-and-spike structure is quite prominent. The spikes grow rapidly in amplitude and the classical tip spreading is well developed at the shoulders of the spikes by 9.2 ns. As the spikes accelerate, lateral flow continues to widen the tips until the foil fragments at 10.6 ns.

The tipreading is due to the nonlinear phase of the Kelvin-Helmholtz instability in the shear layer at the interface between the falling spike and the rising bubble. That a very strong shear layer develops between the bubble and the spike is evident in the vector fluid velocity field (Fig. 6) spanning the region between the arrows on the density contour plots of Fig. 4. The vector lengths are scaled to the maximum velocity (VELMAX) as indicated on each figure.

The lateral flow that causes the tip widening is clearly apparent in the velocity plots. Also note the strong circulatory flow (vortex flow) that develops on the spike side of the shear interface. Although no spiral roll-up appears in the wake of the bulge, the existence of vortex motion is indicated by the non-curl free nature of the fluid flow at the spike shoulders and the flattening of the rear of the bulge.<sup>3</sup>

The time evolution of the bubble-and-spike formation is shown in Fig. 7. Up to about 10 ns the growth of the spike outpaces that of the bubble. Initially the spike experiences less drag than the bubble since the "heavy" spike is replacing fluid with a smaller density whereas the "light" bubble is attempting to rise through a denser medium. It is not until the area of the bubble becomes quite large, thereby increasing its buoyancy, that the bubble velocity approaches the spike velocity.

The amplitude of the bubble-and-spike formation ( $\Delta X_{bs}$ ) is plotted as a function of time in Fig. 8. Here we have also plotted the distance from the critical surface to the spike tip ( $\Delta X_{cs}$ ) and the distance from the rear of the foil to the bubble ( $\Delta X_{rb}$ ) - a measure of how far the bubble has "risen". The spike "falls" nearly exponentially up to saturation at about

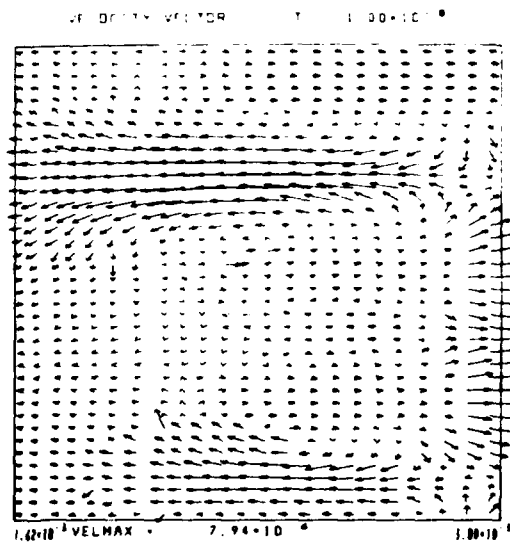
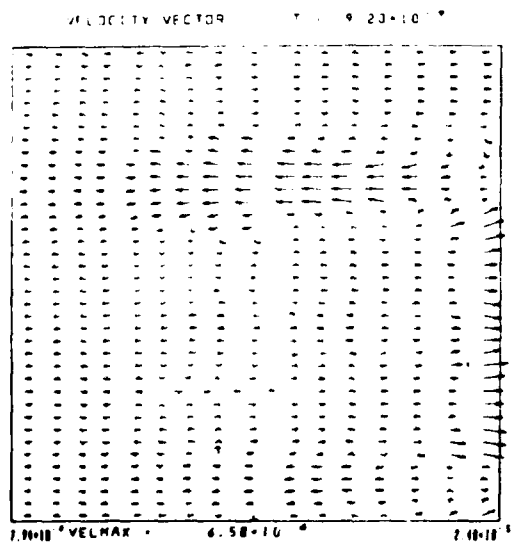
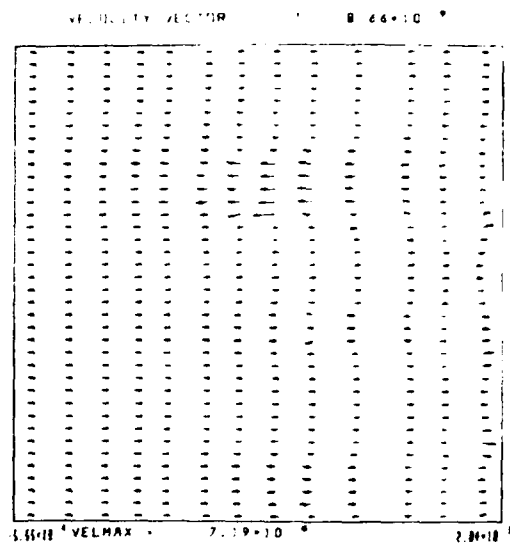
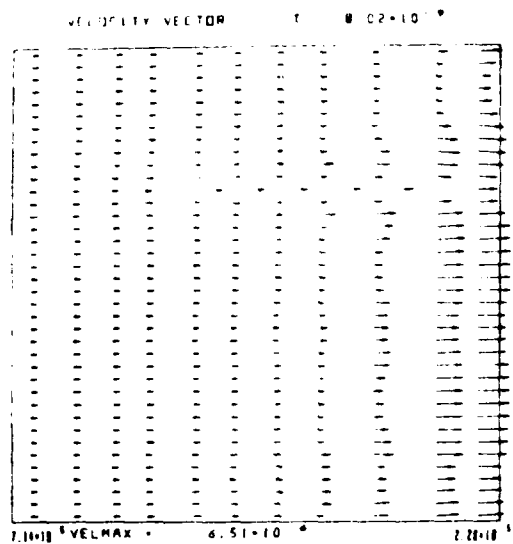


Fig. 6 — Vector fluid velocity plots for the region spanned by the vertical arrows of Fig. 4. In each figure, the vector length is scaled to the maximum velocity (VELMAX). Note the vortices developing at the bubble-and-spike interface at 9.2 and 10 ns.

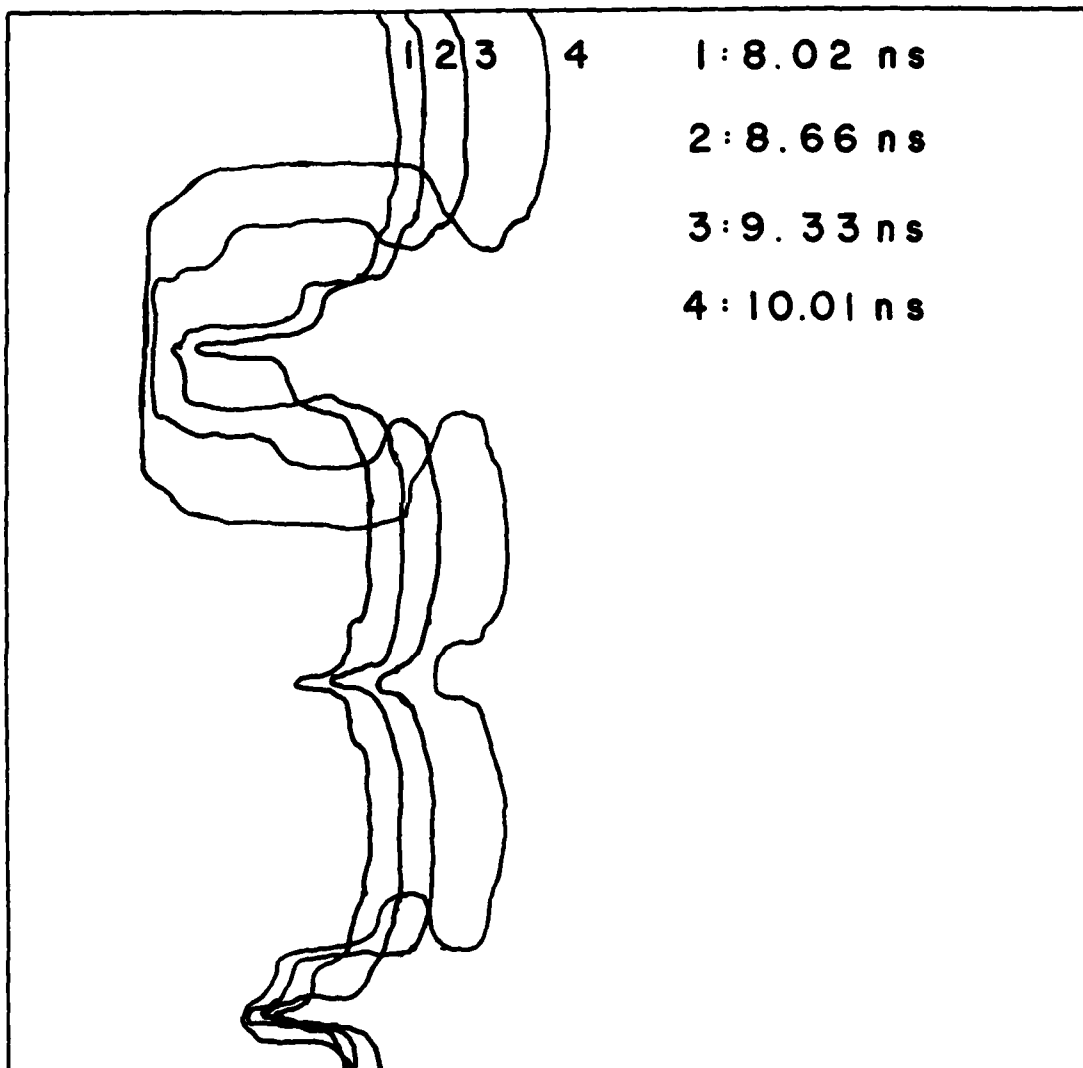


Fig. 7 — Bubble-and-spike contours at various times. Note the large increase in the area of the bubble between 9.33 and 10.01 ns.

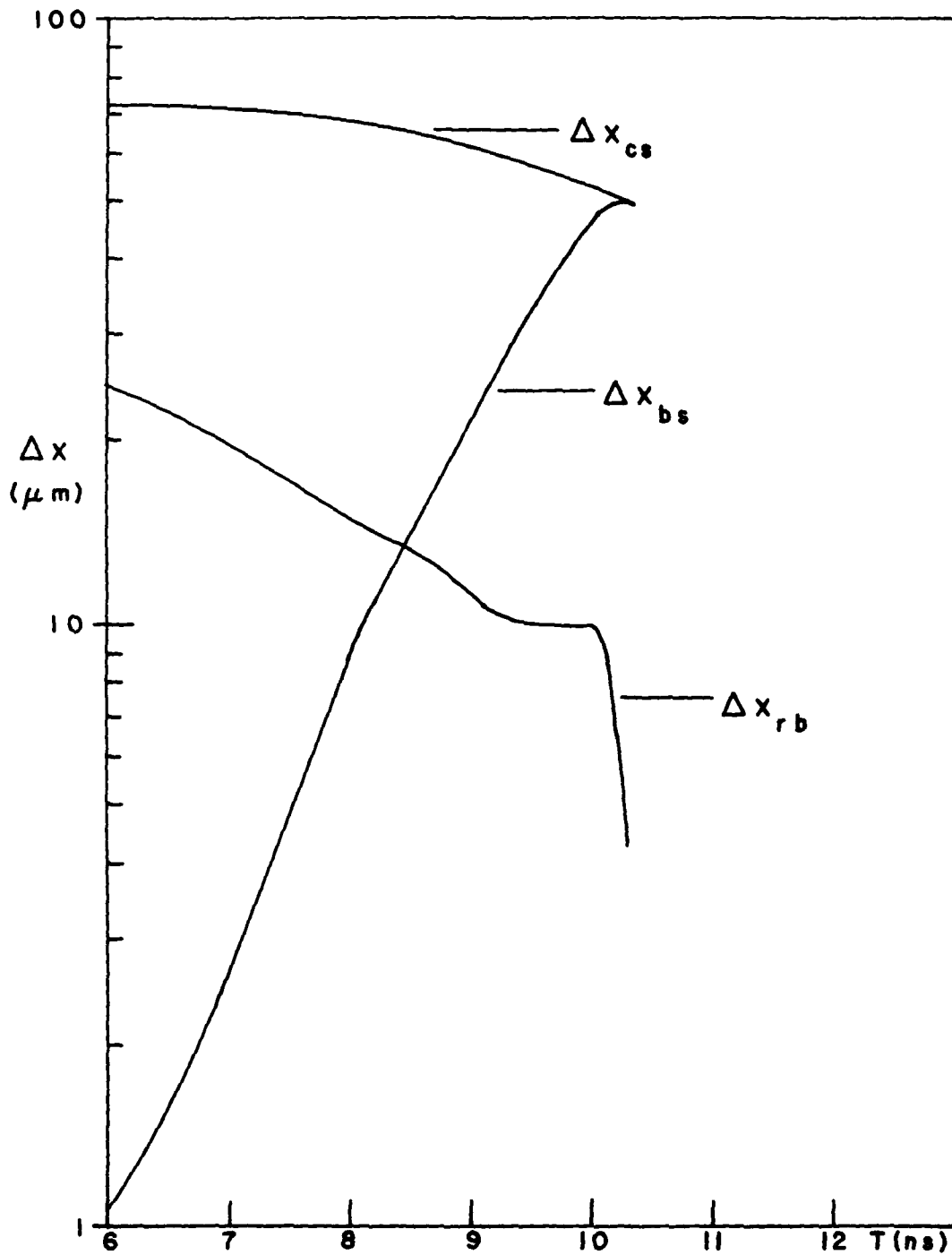


Fig. 8 - A plot of the spike amplitude ( $\Delta X_{bs}$ ), the distance between the critical surface and spike tip ( $\Delta X_{bc}$ ) and the distance between the rear of the foil and the bubble ( $\Delta X_{rb}$ ) as a function of time

10 ns. Note the reduction in the spike growth rate after 8 ns. It is at about this time that the tip-widening appears. The bubble "rise" is much slower and approaches zero between 9 and 10 ns. During this period the area of the bubble is increasing radically (see Fig. 7) until the bubble bouyancy is large enough, coupled with the reduced mass of the shell due to ablation, that the bubble bursts through the rear of the foil.

The temperature contours, Fig. 9, indicate a strong temperature gradient at the spike tip, corresponding to a large mass-ablation rate there; albeit, not large enough to cause a recession of the spike growth.<sup>7</sup> Note that the temperature of the bubble is quite cold and uniform, thus mass ablation must be removed from consideration as a possible stabilizing mechanism for the K-H instability that appears at the spike-bubble interface.

The K-H instability is, in fact, the stabilizing mechanism here. The spike tip widening is due to the growth of the K-H instability in the shear layer at the bubble-and-spike interface. This tip widening increases the frontal area of the spike, thereby increasing its drag and reducing its rate of "fall". With a thicker shell the spike tips may widen enough to seal off the bubble and form a uniform ablation front thereby saturating the spike growth well before shell fragmentation. This aspect of the problem is now being investigated and is the subject of a future report.

Since the growth rates of the instability are well below the classical values, at 10. ns the rear of the foil is still being accelerated uniformly, as shown by the pressure contour in Fig. 10. At this time the foil velocity is 160 km/s - within the range required for inertial fusion. The foil has been pushed a distance of 800  $\mu\text{m}$  - forty times its original thickness.

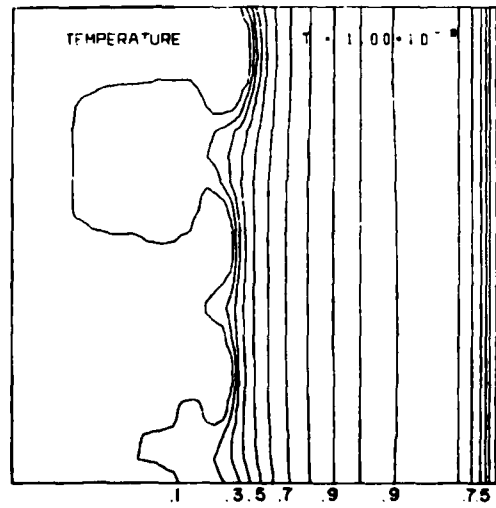
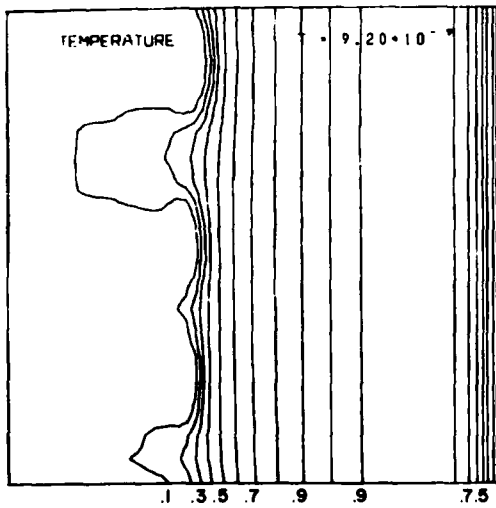
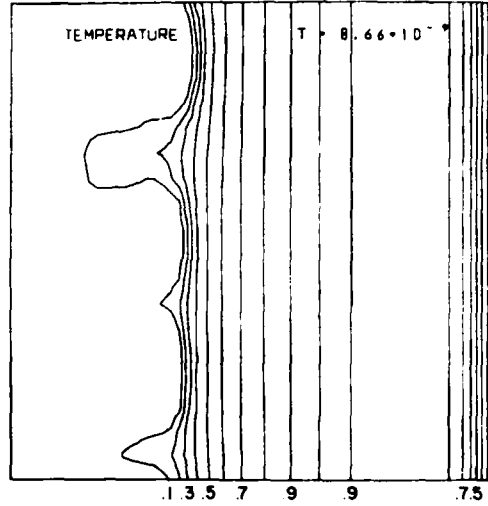
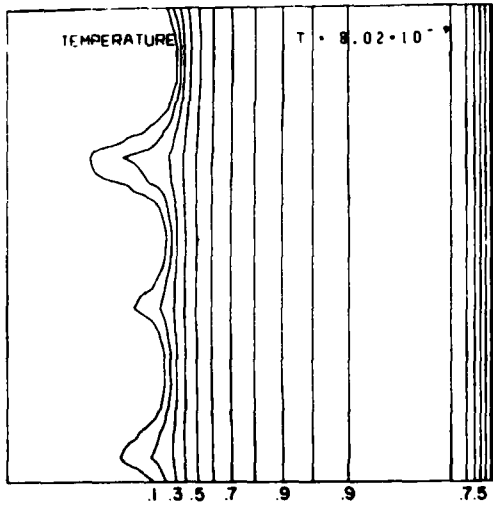


Fig. 9 — Temperature contours corresponding to Figs. 4-6

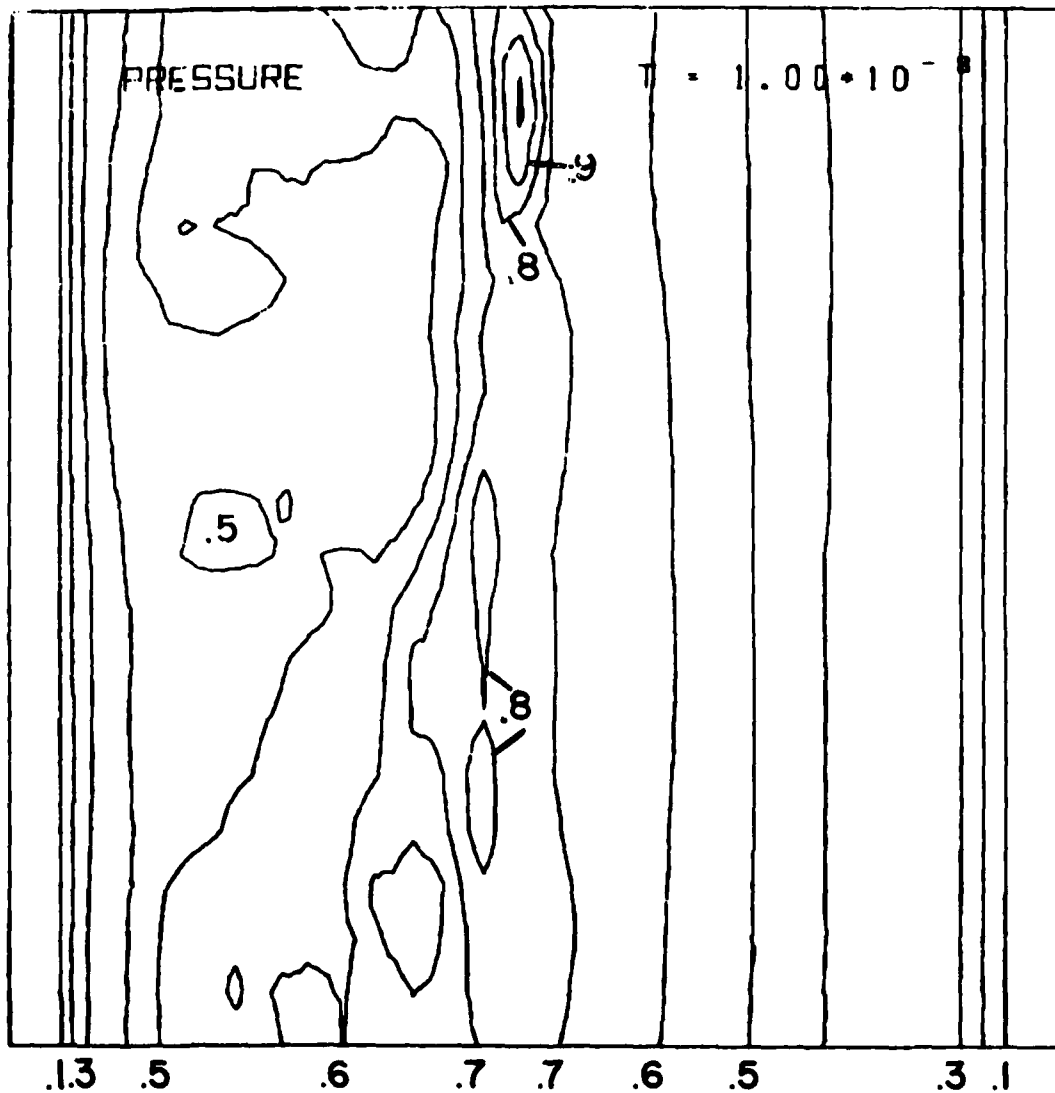


Fig. 10 - Pressure contours at 10 ns. Note that the three leftmost contours are parallel indicating a uniform acceleration of the rear of the foil.

#### IV. SUMMARY

In summary, using the FAST2D laser-shell simulation model we have accelerated a 20  $\mu\text{m}$  thick plastic foil up to 160 km/s. The foil maintained its integrity up to 10. ns giving an aspect ratio of 40. We are able to follow the Rayleigh-Taylor bubble-and-spike development far into the non-linear regime and beyond the point of foil fragmentation. Strong shear flow develops at the interface between the bubble-and-spike which leads to the development of the Kelvin-Helmholtz instability. The K-H instability causes the tips of the spikes to widen and as a result reduce their rate of "fall". This tip widening is a possible stabilization mechanism for the R-T instability for a thicker foil in that the spike tips may widen enough to seal off the bubble and form a uniform ablation front.

The nonlinear aspects of these results differ from those of Ref. 7. We believe there may be several reasons for this difference. The laser intensities used by Ref. 7 are two orders of magnitude larger than the intensities used here. This would result in a much larger mass ablation rate and could possibly explain the spike erosion that they cite. However, since the distance from ablation to critical scales as the laser intensity, their ablation layer should be on the order of 3-5 mm away from the critical surface. Coupled with this large separation between the ablation and critical surfaces is a temperature gradient scalelength at the ablation surface on the order of  $6-12 \mu\text{m}^{16}$  for a 3  $\mu\text{m}$  carbon slab and a laser irradiance of  $10^{15} \text{ W/cm}^2$ . It is difficult to understand how the mass ablation rate could be sensitive to a spike less than a micron in length. Another reason may stem from the difference in the numerical algorithms.<sup>17</sup>

### Acknowledgements

The authors gratefully acknowledge the helpful conversations with S. Bodner, J. Grun, M. Herbst and B. Ripin at NRL. One of us (MHE) especially thanks A. L. Cooper and M. J. Fritts at NRL for our many stimulating discussions and extends a deep appreciation to M. Fry of SAI for the use of his vector plotting routine. This research was supported by the U. S. Department of Energy.

### References

1. Lord Rayleigh, *Theory of Sound* (Dover Publications, Inc., New York, 1894), 2nd ed., Vol. 2; G. I. Taylor, *Proc. Roy. Soc. (London)* A201, 192 (1950).
2. F. H. Harlow and J. E. Welch, *Phys. Fluids*, 9, 842, (1966).
3. B. J. Daly, *Phys. Fluids*, 10, 297, (1967).
4. H. Helmholtz, *Phil. Mag.*, Ser 4, 36, 337, (1868); Lord Kelvin, *Hydrodynamics and General Dynamics* (Cambridge University Press, Cambridge, 1910), p. 69ff.
5. J. D. Lindl and W. C. Mead, *Phys. Rev. Letters*, 34, 1273, (1975).
6. K. A. Brueckner, S. Jorna and R. Janda, *Phys. Fluids*, 17, 1554, (1974).
7. R. L. McCrory, L. Montierth, R. L. Morse and C. P. Verdon, *Phys. Rev. Letters*, 46, 336, (1981).
8. J. P. Boris, *Comments on Plasma Physics and Controlled Fusion*, 3.1, (1977).
9. M. H. Emery, J. H. Orens, J. H. Gardner and J. P. Boris, *NRL Memo Report 4500* (1981). (Submitted to *Phys. Rev. Lett.*).
10. J. P. Boris and D. L. Book, *Methods of Comp. Phys.*, 16, 85, (1976).
11. R. C. Kirkpatrick, *Proceedings of the Topical Conference on Symmetry Aspects of Inertial Fusion Implosions*, Washington, D. C. (1981). (to be published).
12. J. H. Orens, *NRL Memo Report 4167* (1980).
13. P. H. Moffa et al., *Bull. Am. Phys. Soc.*, 24, 946, (1979).
14. R. L. McCrory, T. R. Morse and K. A. Taggart, *Nucl. Sci. Eng.*, 64, 163, (1977).
15. D. Y. Hsieh, *Trans. ASME 94D*, 160, (1972).
16. R. L. McCrory, L. Montierth, R. L. Morse and C. P. Verdon, *Univ. of Rochester, LLE Rept. No. 103*, (1980).
17. M. J. Fritts, E. W. Miner and O. M. Griffin, *Computer Methods in Fluids* (Pentech Press, London, 1980), p. 10ff.